Journal of Physics D: Applied Physics

PAPER • **OPEN ACCESS**

Potentiation and depression behaviour in a two-terminal memristor based on nanostructured bilayer ZrO_x/Au films

To cite this article: Filippo Profumo *et al* 2023 *J. Phys. D: Appl. Phys.* **56** 355301

OPEN ACCESS
IOP Publishing
Journal of Physics D: Applied Physics
J. Phys. D: Appl. Phys. **56** (2023) 355301 (8pp)
https://doi.org/10.1088/1361-6463/acd704

Potentiation and depression behaviour in a two-terminal memristor based on nanostructured bilayer ZrO_x/Au films

Filippo Profumo, Francesca Borghi, Andrea Falqui and Paolo Milani*

CIMAINA and Dipartimento di Fisica "Aldo Pontremoli", Università degli Studi di Milano, Via Celoria 16, Milano 20133, Italy

E-mail: paolo.milani@mi.infn.it

Received 9 February 2023, revised 5 May 2023
Accepted for publication 19 May 2023
Published 1 June 2023

Abstract

The emulation of synaptic functions such as potentiation and depression is of strategic importance for the development of artificial neuromorphic architectures. Memristors can qualitatively reproduce the short-term plasticity behaviour of biological synapses by exploiting the gradual relaxation of resistance levels upon the removal of the switching signals. Various types of memristors based on nanofabricated metal-oxide-semiconductor stacks have been proposed for this purpose. Here we present a different fabrication approach based on cluster-assembled nanostructured zirconia and gold films (ns-Au/ZrO_x) deposited in a bilayer planar configuration. This device shows memristive behaviour with short-term memory and potentiation/depression. The observed relaxation can be described by a stretched-exponential function. Furthermore, the characteristic time of the short-term phenomena dynamically changes under repeated pulses application. Our nanostructured device is characterised by a substantially larger conductive path length with respect to other nanoscale memristive devices; the use of a zirconia nanostructured film makes the device compatible with neuronal cell culture.

Supplementary material for this article is available online

Keywords: memristor, nanostructured films, synapse, neuromorphic system

(Some figures may appear in colour only in the online journal)

1. Introduction

Memristors are effective building blocks for resistive random access memory (RRAM) devices and neuromorphic computing systems: their resistive switching (RS) properties and non-volatility after the removal of the applied switching voltage are suitable for data storage applications [1, 2]. On the other hand, memristors can qualitatively implement some of the synaptic functions due to the capacity to change their electrical conduction state by transitory information crossing [1, 3]. In particular, memristors, showing resistance levels gradually relaxing toward a thermodynamically stable state upon the removal of the switching signal, provide the possibility of emulating the short-term plasticity of biological synapses [4, 5].

In view of the realisation of interfaces between artificial and biological neural networks, there is a growing interest in the direct coupling of memristive devices and networks with *in vitro* experiments with biological cells or tissues [6–8]. Typically memristors have a two-terminal structure consisting

* Author to whom any correspondence should be addressed.

of a switching layer sandwiched between two metallic electrodes. The switching layer ranges from semiconducting to insulating inorganic or organic materials [9], according to the phenomena involved in RS activation. They can be fabricated using standard lithographic methods, however the managing of the interface with biological systems may require a planar configuration with dimensions larger than those typical of microelectronics [7, 10].

Among a large number of metal oxides showing RS, ZrO_2 received considerable attention owing to its belonging to high-k dielectrics with high permittivity, simple composition, easy fabrication, and its compatibility with standard complementary metal-oxide semiconductor (CMOS) fabrication processes [11, 12]. ZrO_2, ZrO_x and Yttrium-stabilized zirconia with thicknesses between 10–100 nm are used with different types of electrodes [11, 13–19].

Memristors based on zirconia layers show unipolar and bipolar RS between a high resistance state and a low resistance state [13]. This electrical behaviour is ascribed to different conduction mechanisms based on the drift of oxygen ions and oxygen vacancies in the external electric field applied between the electrodes [20]; this causes the formation of conducting filaments at the nanoscale that undergo continuous formation and rupture [21].

Several authors proposed to modify zirconia films with metallic ions or nanoparticles to improve the low device reproducibility, make their electric properties more stable, and avoid the need for a forming process to induce the RS behaviour [14–16, 18, 19]. Implantation of Zr, Ti and Au ions into the zirconia film allowed the actual fabrication of devices with more stable and reproducible RS behaviour, improved R_{on}/R_{off} ratio, faster set/reset processes, eliminating the need for a forming process [15–17]. Guan *et al* reported a device with bipolar RS consisting of a zirconia layer with embedded Au nanoparticles to improve the device yield [14]. The embedding of Co nanoparticles was also reported leading to lower $V_{forming}$ and V_{set} [18]. Filatov *et al* exploited Au islands in an underlying layer to concentrate electric field and therefore filament formation [19].

In order to emulate the plasticity behaviour, including spike-timing-dependent plasticity typical of biological synapses, oxide-based second-order memristors can be used by exploiting the different time scales of internal ionic dynamics [4]. Planar devices based on tungsten oxides [3] and Au/SiO_xN_y:Ag/Au demonstrated short- and long-term plasticity typical of biological synapses [4]. In the latter case, the switching mechanism was attributed to the diffusion and reversible coalescence of metallic nanoparticles embedded in the insulating matrix due to joule effects induced by current pulses.

Here we propose an approach to the fabrication of planar memristive systems showing short-term plasticity and with structural characteristics compatible with the conditions of *in vitro* cell culture and microscopy experiments, including a good optical transparency of the entire device. The system consists of the superposition of two layers: the bottom one made of a cluster-assembled gold film and the top one of a cluster-assembled zirconia film. We already reported the non-ohmic electrical behaviour of gold cluster-assembled films (CAFs) [22, 23]; by coupling gold and zirconia CAFs, we characterised the time evolution of their non-linear behaviour in a large device (4 mm conductive path length) with particular attention to depression and potentiation phenomena and electric carrier dynamics. The nanostructured zirconia topmost layer is biocompatible and suitable for the culture and manipulation of neuronal cells [24, 25].

2. Methods

2.1. Device fabrication

In view of the coupling of the devices with cell cultures, we used glass coverslips as substrates. Glass has a very low electrical and thermal conductivities that prevent interference in the characterisation of high resistivity nanostructured films. Ns-Au/ZrO_x bilayer films were deposited on a commercial glass coverslip (Zeus 2 cm × 2 cm × 1 mm), cleaned by 15 min sonication in ethanol where two gold electrodes separated by a 4 mm long gap, with a thickness of 80 nm and dimensions of 3 mm × 7 mm, are deposited by thermal evaporation. A gold nanostructured film (ns-Au) and, subsequently, a zirconia (ns-ZrO_x) nanostructured film, respectively of 30 nm and 90 nm thickness, were deposited using a supersonic cluster beam deposition (SCBD) apparatus equipped with a pulsed microplasma cluster source (PMCS) that allows the production of neutral clusters in the gas phase as described in details in [26]. Briefly, the PMCS principle of operation consists in the ablation of a gold or zirconia target by a plasma ignited during the injection of a high-pressure pulse of argon in the aggregation chamber of the cluster source [27]. The species resulting from the target ablation condense in the source chamber through collision with the Argon gas forming clusters, and then the cluster-gas mixture is expanded through a nozzle resulting in a supersonic seeded beam [27]. The cluster beam is focused by an aerodynamic lens system and directed in the deposition chamber (figure 1(a)), where the substrates are mounted on the sample holder. Glass substrates are masked by a metallic stencil mask (200 μm thick) with a central rectangular hole (1 mm × 7 mm). We used the same mask for both the ns-Au and the ns-ZrO_x depositions, obtaining a layered structure. The ns-Au/ZrO_x films are represented schematically, in the top view in figure 1(b) and in the cross-section view in figure 1(c).

2.2. Structural characterisation

Transmission electron microscopy (TEM) images and the corresponding electron diffraction patterns (EDPs) were acquired by using a ThermoFischer Talos 120 C microscope operating at an acceleration voltage of 120 kV, equipped with a thermionic LaB6 electron source and a bio-twin objective lens.

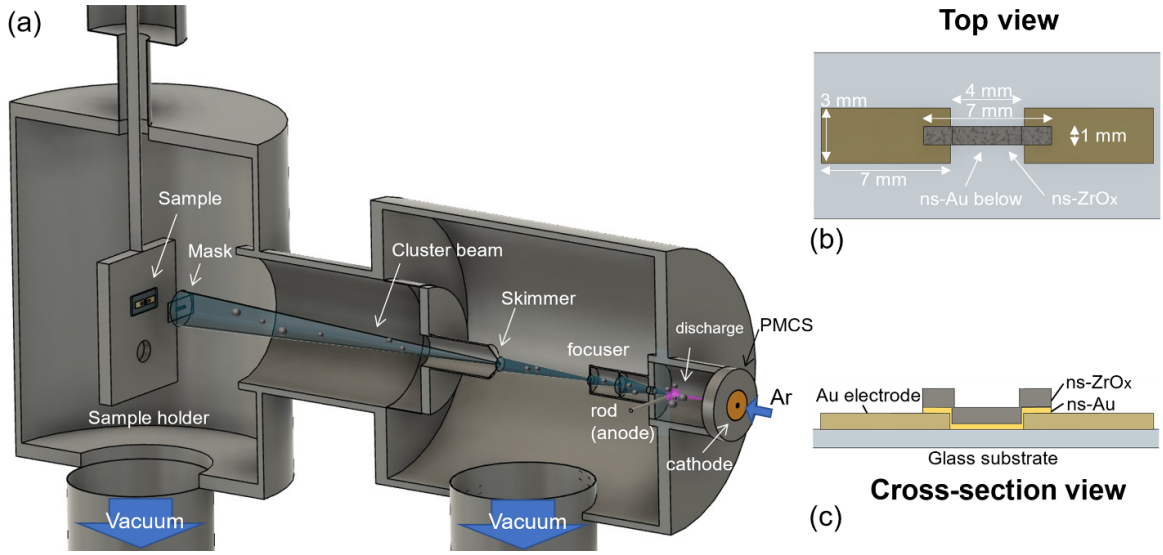

Figure 1. (a) Schematic view of the SCBD apparatus. Clusters are formed in the PMCS. The cluster beam is extracted through the aerodynamic focuser, and then it reaches the skimmer in the expansion chamber, leading the clusters into the deposition chamber. Here a masked glass substrate is mounted. On the right, sketches of the produced two-terminal devices are shown. (b) Top view of a ns-Au/ZrO_x sample made by a 1 mm large nanostructured Au/ZrO_x layered film connecting two PVD gold electrodes on a glass sample. (c) Cross-section view of the same device shown in panel b (not to scale).

Both images and EDPs were collected by a Ceta CMOS camera (4096 × 4096 pixels).

The morphological investigation of the nanostructured films was performed by a Multimode 8 AFM (Bruker), in peak-force tapping mode, equipped with silicon nitride cantilevers mounting single crystal silicon tips, with nominal radius 12–20 nm, resonance frequency in the range 100–200 kHz, and force constant $k = 0.7$ N m^{-1}. All the topographic maps have been collected with a sampling resolution of 1–5 nm pixel^{-1}, using a scan rate of approximately 1 Hz. From flattened AFM images, the root-mean-square surface roughness Rq was calculated as the standard deviation of surface heights.

2.3. Electrical characterisation

Ex-situ electrical characterisation was performed with a high precision measurement system (Agilent E5270B electrometer equipped with an E5287A high resolution Atto Level sensor) via a standard two-probes method. Data were acquired using a custom software developed in LabView. The characterisation of the film resistance and switching properties was performed by means of repeated current measurements, with the samples biased with voltages varying according to a stepped triangular ramp (i.e. a piecewise input voltage) to derive the characteristic I–V curve of the two terminal devices.

In addition to constant voltage measurements, we used pulse measurements to study the effect of limited duration stimuli on sample behaviour. Pulsed measurements are often exploited in literature to characterise RRAM devices, where read and write pulses are used to monitor the resistive state of the sample or to control it stimulating switching phenomena, respectively. Two different types of pulses were used:

(i) write pulses at high positive or negative voltages (ranging between 5 V and 20 V), meant to change the sample's resistance
(ii) read pulses at a fixed voltage of 1 V, to detect the change of the conductive properties of the samples induced by write pulses

We used the Agilent E5270B configured to execute quasi-continuous pulsed measurements (many measurements taken during every pulse); this characterisation allowed to perform an investigation closer to the actual operation modes of a memory storage device, where information is accumulated or detected with rapid voltage signals.

3. Results and discussion

3.1. Film morphology and structure

3.1.1. Atomic force microscopy characterisation. Figure 2 reports the typical nanoscale morphology of the films, before and after electrical characterisation; for the sake of comparison, ns-Au film (figure 2(a)) is also shown. Ns-Au and ns-Au/ZrO_x are both characterised by a porous and granular structure at the nanoscale, whose roughness evolves with thickness according to a simple scaling law [28], characterised by almost the same growth exponent for both the materials [29, 30]. The ns-Au (30 nm thick) film shows a calculated roughness $Rq = 10.5 \pm 0.2$ nm (figure 2(a)), whereas the layered ns-Au/ZrO_x (30 nm/90 nm) has an

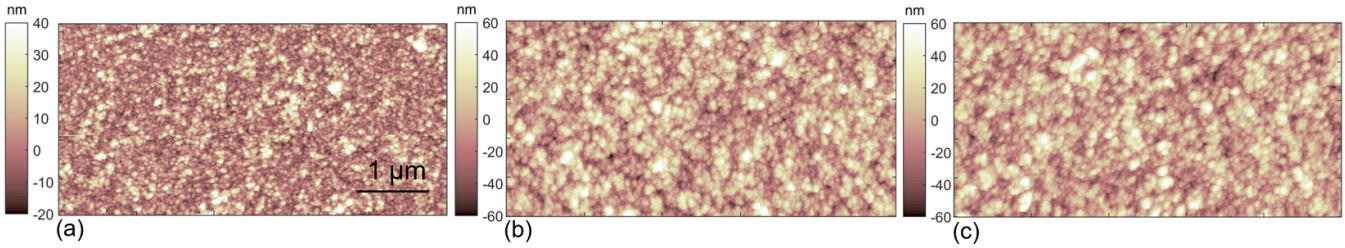

Figure 2. AFM morphological maps. From left to right: (a) ns-Au film as deposited, (b) layered ns-Au/ZrO_x film and (c) same film after electrical stress.

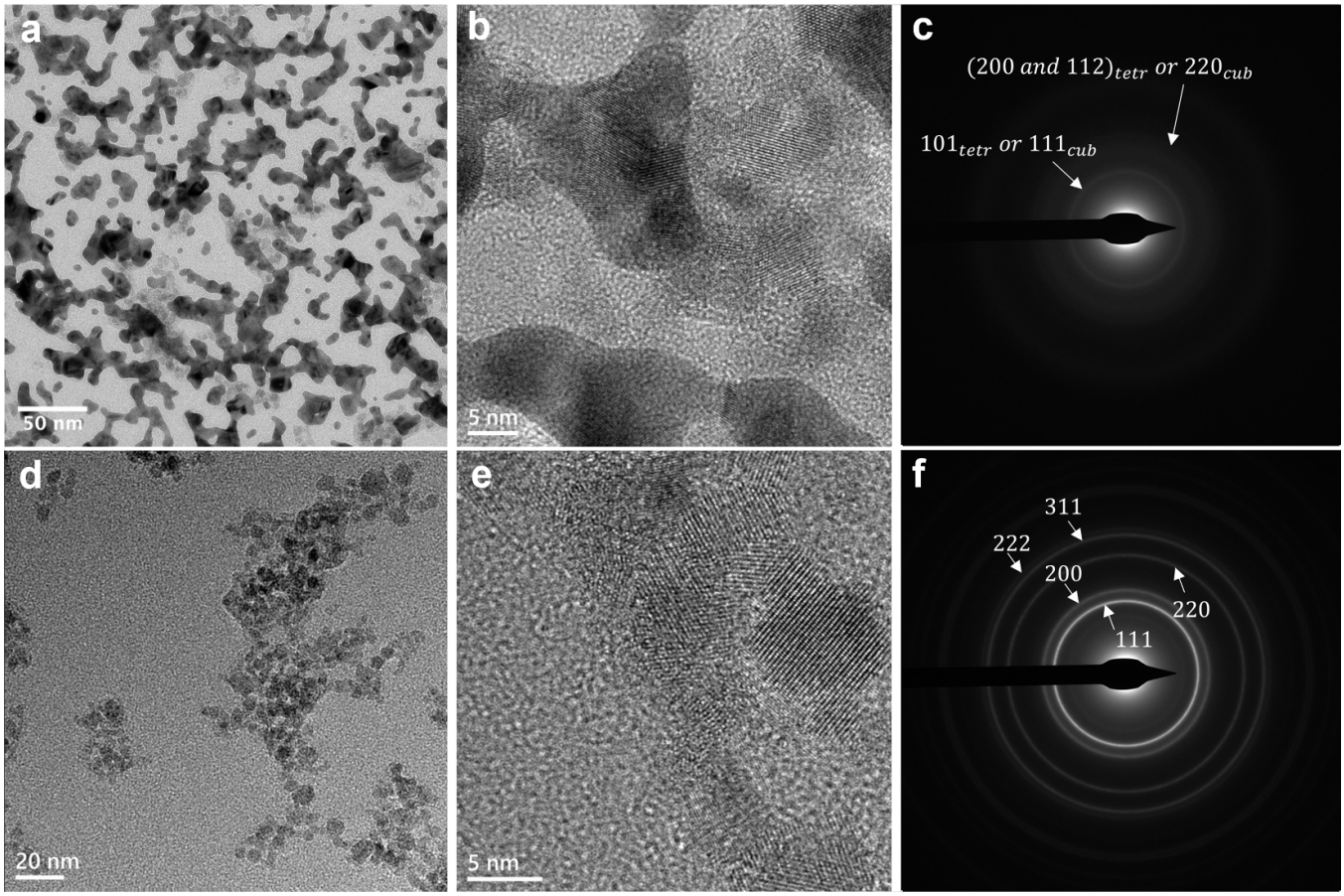

Figure 3. TEM/HRTEM imaging and electron diffraction pattern (EDP) of a ns-ZrO_x sample (a)–(c) and a layered ns-Au/ZrO_x sample (d)–(f). Panels a and d display low-magnification TEM images of the two samples, while panels b and e show the corresponding HRTEM imaging. EDPs are reported in panels c and f, respectively indexed with the corresponding lattice sets of the most likely ZrO_2 phase and fcc gold.

$Rq = 20.1 \pm 0.3$ nm (figure 2(b)). A ns-Au/ZrO_x layered film after electrical forming and characterisation (see section 3.2.1) is shown in figure 2(c). This film has $Rq = 20.6 \pm 0.4$ nm, substantially comparable to the Rq measured for an 'as deposited' layered film (figure 2(b)); no electrically induced changes in the morphological features are present at the nanoscale.

We also performed environmental scanning electron microscopy characterisation close to the electrodes/nanostructured film interface to rule out high field-related reconstructions of the layered nanostructured film. No significant modification of the film morphology is present, as shown in supplemental figure S1.

3.1.2. Nanoscale structure. We deposited low-coverage thin films on TEM grids to characterise their structure. Two samples, the first one constituted by sole ns-ZrO_x (5 nm thick) and the second one by ns-Au (10 nm thick) and ns-ZrO_x (5 nm thick), were deposited on 12 nm-thin amorphous carbon grids. Together with the TEM/high-resolution trasmission electron microscopy (HRTEM) images, the corresponding EDPs have

also been acquired to determine the most likely crystal structure of the nanoparticles constituting the films. In figures 3(a)–(c) the TEM/HRTEM images and the EDP from zirconia, and (d)–(f) by the sample containing both zirconia and gold, are shown. The TEM/HRTEM imaging clearly indicates that both samples are characterised by nanosized objects (panels (a) and (d) for low magnification TEM, panels (b) and (e) for HRTEM), which preserve their granularity after deposition on the substrate and form fractal-like structures. The EDPs, obtained by selecting a large area of each sample, show that the nanosized objects are constituted by crystal domains. Here, as expected, only two relatively weak diffraction rings were observable for the sample containing sole zirconia phase (panel (c)) and correspond to an interplanar distance of 2.9 $\pm$ 0.1 Å and 1.8 $\pm$ 0.1 Å, respectively, being the first one the most intense. It corresponds to the most intensely diffracting lattice set for both the zirconia tetragonal (101) and cubic (111) phases. The second and weaker ring, found at 1.8 $\pm$ 0.1 Å, is again shared between the two zirconia phases, corresponding to the superposing (112) and (200) lattice sets of the tetragonal phase, and the (220) lattice set of the cubic phase. However, the concomitant absence of a diffraction ring at a distance of 3.16 Å, allows ruling out the presence of zirconia in the monoclinic phase, as the latter should show its most intense ring at that distance and should not display visible rings at 2.96 Å, which is conversely clearly observed in both samples. These results are in agreement with the XRD measurements performed on nanostructured zirconia, provided in [31], which particularly stress the presence of the cubic phase in zirconia at room temperature.

The EDP of the layered sample constituted by both zirconia and gold (panel (f)) shows clearly all the rings expected for the fcc gold (indexed in that pattern), together with those found already for the sole zirconia, and here not indexed for the sake of simplicity.

3.2. Electrical characterisation

3.2.1. Current—voltage analysis. The as-deposited layered ns-Au/ZrO_x films show an ohmic electrical behaviour characterised by a linear *I–V* curve (see supplementary figure S2(b)), as also the sole as-deposited ns-Au films [22, 32]. However, the addition of the zirconia layer decreases the resistance value of the composite sample, as it is shown in supplementary figure S2(a). By applying a high constant voltage (approximately 16 V) to the composite ns-Au/ZrO_x sample an abrupt forming process occurs. The layered ns-Au/ZrO_x film shifts to an irreversible high-resistance state, while the ns-Au film passes through the device's breakout as shown in supplementary figure S2(c). This high-resistance state shows a memristive behaviour with hysteresis loops in *I–V* curves (figure 4). Here, three *I–V* curves at 1 V s^{-1}, 2.5 V s^{-1}, and 5 V s^{-1} sweep velocities are reported. The greater the sweep velocity, the greater the current passing through the device. This effect can be attributed to charged migrating species [33, 34], originating from defects into the zirconia overlayer, and modifying the conductivity of the device. Furthermore, current spiking activity, ascribable to the ns-Au film switching activity, appears at applied voltages over 10 V (figure 4). Reference samples made by a 50 nm thick ns-ZrO_x show an ohmic conduction regime with resistance of the order of 5 10^{11} Ω (see figure S3), suggesting that the memristive effect, together with non-linearity registered for the layered samples, is induced in ns-ZrO_x by the presence of the nanostructured gold film.

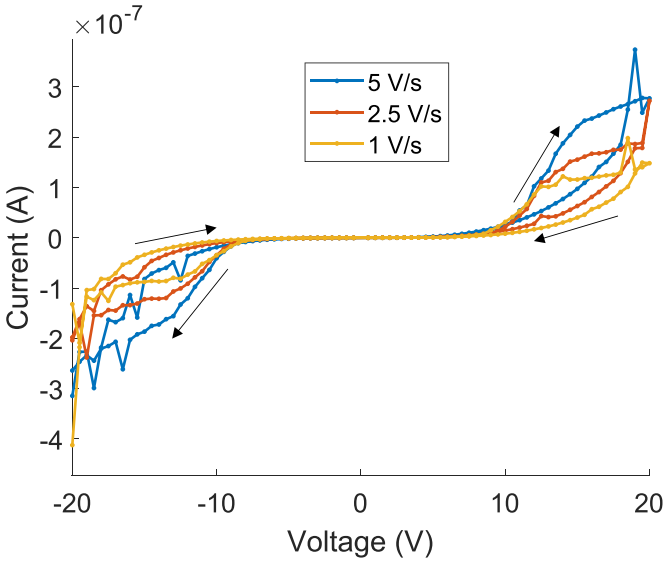

Figure 4. DC *I–V* curves of a layered ns-Au/ZrO_x sample after resistive switching activation, taken with different sweep velocities (1 V s^{-1}, 2.5 V s^{-1} and 5 V s^{-1}). A memristive hysteresis loop is registered, and current through the device (nonlinearity of the device response) increases with increasing sweep speeds. Black arrows specify the curve path direction.

3.2.2. Pulsed voltage analysis. The possibility of controlling the resistance of the layered devices has been studied by means of a pulsed analysis, where alternated write pulses are alternated with read pulses. We observed that the resistance measured with read pulses with the same polarity of the write pulses is about one order of magnitude larger than that measured with read pulses with an inverse polarity ($R_{on/off} \sim 10$, see figure 5). This could be explained by considering that oxygen vacancies in the ns-ZrO_x layer under write voltage application can diffuse towards the cathode electrode interface and create a negative charge gradient in the CAF. Read pulses with opposite voltage polarity can then modify the gradient, facilitating electronic charge injection. We underline that the presence of the ns-Au layer is necessary to observe this behaviour, whereas ns-ZrO_x films do not show such an intense response to the application of voltage pulses (see supplementary figure S4).

The resistance measured during the read pulses shows a transient increasing behaviour on the timescale of seconds, suggesting the presence of diffusion-driven conduction [4] and demonstrating the device's volatile nature [1]. In figure 5, write pulses of $\pm$5 V (100 ms in width) and +1 V read pulses (500 ms in width) are reported (bottom), with the resistance measured during each read pulse (top) (the sampling

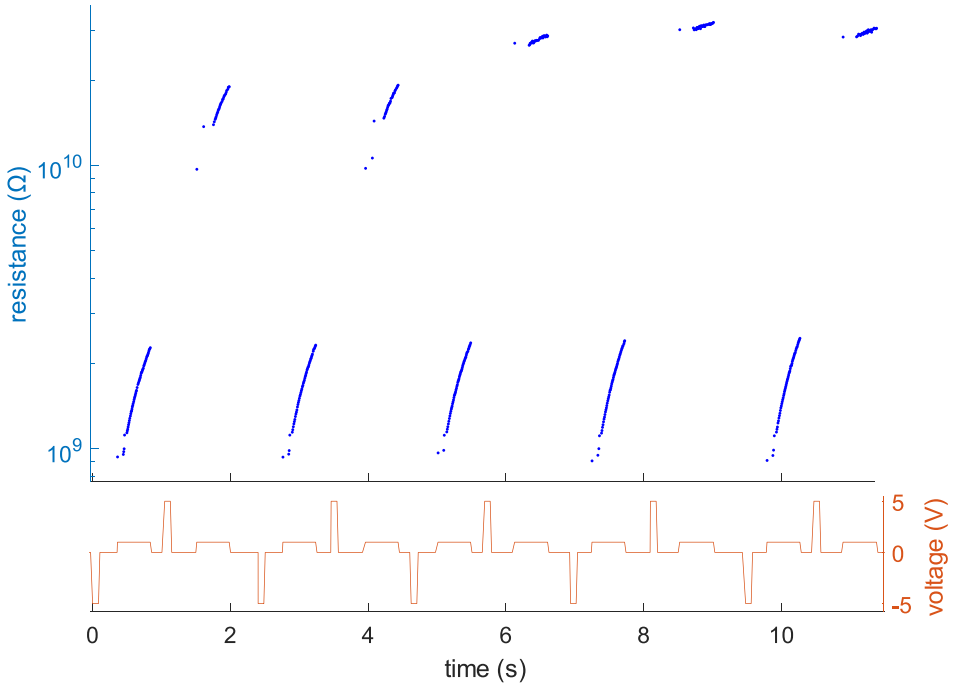

Figure 5. Resistance modulation by application of 5 V (100 ms in width) write pulses with alternated polarity, interspersed with 1 V (500 ms in width) read pulses on a layered ns-Au/ZrO_x sample. The resistance measured during read pulses (top) and the applied voltage (bottom) are reported in the same figure. Resistance after negative write pulses is about one order lower with respect to that registered after positive write. During every read pulse the resistance has a transient increasing trend.

frequency is 150 Hz, and the initial measurements are up to 100 ms long due to the instrument's initial settings). The resistance switches between 1 GΩ and 10 GΩ with an increasing transient behaviour (resistance is increased by about a factor 2 in the first 500 ms). We tested the switching behaviour of the devices between these two levels for more than 100 cycles as reported in supplementary figure S5.

To assess the layered device transient response to pulsed stimuli, current evolution at 1 V applied voltage following a single 100 ms write pulse with negative polarity was recorded. A decreasing current trend on the timescale of a few seconds was observed, in accordance with the trend shown for alternated pulses in figure 5. In [35], a stretched-exponential function (SEF) has been proposed as a model for the spontaneous retention loss of memristors and specifically to study oxygen-related relaxation processes. The SEF is written as:

$$\phi(t) = I_0 \exp\left[-\left(\frac{t}{\tau}\right)^{\beta}\right] \quad (1)$$

where, in our case, $\phi(t)$ is the relaxation function, τ is the relaxation time, I_0 a prefactor and $\beta \in (0,1)$ a stretch index. We found that the same function well describes the layered ns-Au/ZrO_x relaxation curves and that if successive measurements are taken after write pulses, the characteristic relaxation time τ is increased from roughly 10 ms to 1 s. Similar results were obtained for TiO_2 devices as a function of the number of subsequent pulses [36]. This suggests (as also reported in [35]) that the relaxation characteristics can similarly change under repeated pulses as in short-term memory to long-term memory transition in biological systems [37].

Figure 6-left shows three current measurements at 1 V registered after three subsequent write pulses at −10 V applied voltage on a layered ns-Au/ZrO_x film. A decreasing trend on the timescale of seconds is observed. The three curves normalized by the pre-factor I_0 are shown with their fit according to equation (1) in figure 6-right, the second and third curves show a slower decreasing trend corresponding to greater τ fitted parameters (as reported in the table of figure 6).

The ability to change quasi-continuously the conductance of a memristive device with subsequent write pulses with the same polarity is analogous to pulse pair facilitation (PPF) in neurons [5]. The layered ns-Au/ZrO_x device shows current potentiation (depotentiation) when subsequent write pulses and read pulses are alternated with different (same) polarity. This effect can be described by oxygen vacancies diffusion-related accumulation in the device facilitating or suppressing current conduction during read pulses, as proposed in a WO_x memristor [3]. A typical potentiation (depotentiation) trend registered by means of current measurements taken with 1 V read pulses in between 20 subsequent +5 V (−5 V) write pulses is reported in figure 7 (indicated as P: potentiation and D: depression).

The PPF behaviour is typical of natural synapses for signal compression, where information on spikes number and firing rate is stored into gradual changes of the

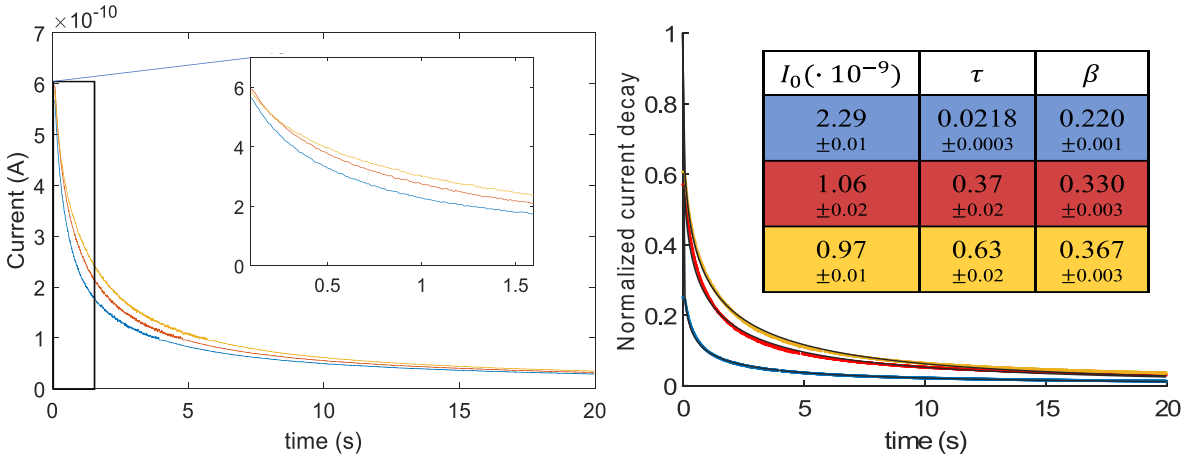

Figure 6. Relaxation for ns-Au/ZrO_x layered devices. Left: current vs time at 1 V constant voltage applied collected after a −10 V 100 ms width write pulse for three subsequent measurements (blue–red–yellow). Inset: zoomed starting portion of the curves highlighting the differences in the first 1.5 s. Right: comparison of the same three curves normalised by the pre-factor I_0. Solid black lines are fitted data according to equation (1). The inset reports the parameters fitted for the three curves (with 95% confidence bounds).

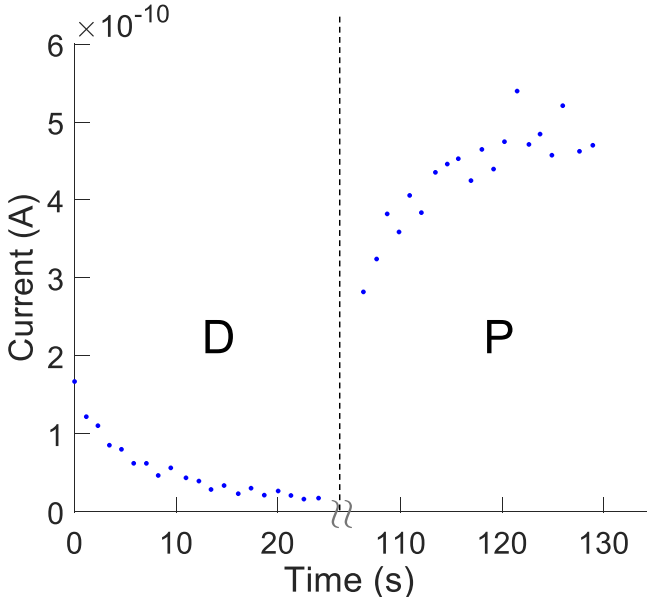

Figure 7. Depression and potentiation behaviours of layered ns-Au/ZrO_x samples. Current depression by application of 20 consecutive −5 V 100 ms width write pulses interspersed with 500 ms 1 V read pulses is depicted on the left. In the same graph, on the right, the subsequent measurements taken with reverse +5 V write voltage polarity are reported.

postsynaptic membrane conductance [38, 39]. The inherent voltage thresholds of our device can be used for discriminating recorded spiking events from background activity and without resorting to computationally heavy off-line processing. Information on spike amplitude and frequency can be transduced and stored in single devices as resistive state transitions, as reported for an array of TiO_x memritors [6].

4. Conclusions

In summary, we reported the fabrication of a planar device based on bi-layered ns-Au/ZrO_x CAFs showing a memristive behaviour. The system exhibits neuromorphic properties such as short-time retention (order of seconds) with stretched-exponential relaxation, and potentiation/depotentiation for subsequent write pulses. The resistance of the film can be controlled by means of voltage pulses of different polarities.

The observed behaviour can be attributed to the presence of two conduction mechanisms related to electron transport in the ns-Au film and ion transport in the ns-ZrO_x layer: ion diffusion inside the ns-ZrO_x insulating layer can produce electrical relaxation phenomena as addressed for SEF relaxation.

The planar structure of the reported device and the presence of a nanostructured zirconia upper layer make this system potentially interesting for the coupling with biological neural networks: the use of nanostructured zirconia films as substrates for the culture of primary neural cells has been recently reported [26].

Data availability statement

All data that support the findings of this study are included within the article (and any supplementary files).

Acknowledgments

We thank Professor A Pullia for making available the Agilent E5270B electrometer used for the electrical characterisation of the devices.

ORCID iDs

Filippo Profumo https://orcid.org/0000-0001-9409-595X
Francesca Borghi https://orcid.org/0000-0001-6980-4910
Andrea Falqui https://orcid.org/0000-0002-1476-7742
Paolo Milani https://orcid.org/0000-0001-9325-4963

References

[1] Zhou G *et al* 2022 Volatile and nonvolatile memristive devices for neuromorphic computing *Adv. Electrochem. Mater.* **8** 2101127

[2] Sangwan V K and Hersam M C 2020 Neuromorphic nanoelectronic materials *Nat. Nanotechnol.* **15** 517–28

[3] Chang T, Jo S-H, Kim K-H, Sheridan P, Gaba S and Lu W 2011 Synaptic behaviors and modeling of a metal oxide memristive device *Appl. Phys.* A **102** 857–63

[4] Wang Z *et al* 2017 Memristors with diffusive dynamics as synaptic emulators for neuromorphic computing *Nat. Mater.* **16** 101–8

[5] Du C, Ma W, Chang T, Sheridan P and Lu W D 2015 Biorealistic implementation of synaptic functions with oxide memristors through internal ionic dynamics *Adv. Funct. Mater.* **25** 4290–9

[6] Gupta I, Serb A, Khiat A, Zeitler R, Vassanelli S and Prodromakis T 2016 Real-time encoding and compression of neuronal spikes by metal-oxide memristors *Nat. Commun.* **7** 12805

[7] Illarionov G A, Kolchanov D S, Kuchur O A, Zhukov M V, Sergeeva E, Krishtop V V, Vinogradov A V and Morozov M I 2019 Inkjet assisted fabrication of planar biocompatible memristors *RSC Adv.* **9** 35998–6004

[8] Serb A *et al* 2020 Memristive synapses connect brain and silicon spiking neurons *Sci. Rep.* **10** 2590

[9] Lanza M, Sebastian A, Lu W D, Le Gallo M, Chang M-F, Akinwande D, Puglisi F M, Alshareef H N, Liu M and Roldan J B 2022 Memristive technologies for data storage, computation, encryption, and radio-frequency communication *Science* **376** eabj9979

[10] Rajan K *et al* 2017 WORM and bipolar inkjet printed resistive switching devices based on silver nanocomposites *Flex. Print. Electron.* **2** 024002

[11] Parreira P, Paterson G W, McVitie S and MacLaren D A 2016 Stability, bistability and instability of amorphous ZrO_2 resistive memory devices *J. Phys. D: Appl. Phys.* **49** 095111

[12] Sun B, Liu Y X, Liu L F, Xu N, Wang Y, Liu X Y, Han R Q and Kang J F 2009 Highly uniform resistive switching characteristics of TiN/ZrO2/Pt memory devices *J. Phys. D: Appl. Phys.* **5** 061630

[13] Jonsson A K, Niklasson G A and Veszelei M 2002 Electrical properties of ZrO_2 thin films *Thin Solid Films* **402** 242–7

[14] Guan W, Long S, Jia R and Liu M 2007 Nonvolatile resistive switching memory utilizing gold nanocrystals embedded in zirconium oxide *Appl. Phys. Lett.* **91** 062111

[15] Liu Q, Guan W, Long S, Jia R, Liu M and Chen J 2008 Resistive switching memory effect of ZrO_2 films with Zr+ implanted *Appl. Phys. Lett.* **92** 012117

[16] Liu Q, Guan W, Long S, Liu M, Zhang S, Wang Q and Chen J 2008 Resistance switching of Au-implanted-ZrO_2 film for nonvolatile memory application *J. Appl. Phys.* **104** 114514

[17] Liu Q, Long S, Wang W, Zuo Q, Zhang S, Chen J and Liu M 2009 Improvement of resistive switching properties in ZrO_2-based ReRAM with implanted Ti ions *IEEE Electron Device Lett.* **30** 1335–7

[18] Wu M-C, Wu T-H and Tseng T-Y 2012 Robust unipolar resistive switching of Co nano-dots embedded ZrO_2 thin film memories and their switching mechanism *J. Appl. Phys.* **111** 014505

[19] Filatov D, Antonov D, Antonov I, Kasatkin A and Gorshkov O 2017 Resistive switching in stabilized zirconia films studied by conductive atomic force microscopy *Mater. Sci. Chem. Eng.* **5** 8–14

[20] Guseinov D V *et al* 2017 Filamentary model of bipolar resistive switching in capacitor-like memristive nanostructures on the basis of yttria-stabilised zirconia *Int. J. Nanotechnol.* **14** 604

[21] Sun W, Gao B, Chi M, Xia Q, Yang J J, Qian H and Wu H 2019 Understanding memristive switching via *in situ* characterization and device modelling *Nat. Commun.* **10** 3453

[22] Mirigliano M, Decastri D, Pullia A, Dellasega D, Casu A, Falqui A and Milani P 2020 Complex electrical spiking activity in resistive switching nanostructured Au two-terminal devices *Nanotechnology* **31** 234001

[23] Mirigliano M, Paroli B, Martini G, Fedrizzi M, Falqui A, Casu A and Milani P 2021 A binary classifier based on a reconfigurable dense network of metallic nanojunctions *Neuromorph. Comput. Eng.* **1** 024007

[24] Previdi A, Borghi F, Profumo F, Schulte C, Piazzoni C, Lamanna J, Racchetti G, Malgaroli A and Milani P 2023 Nanotopography and microconfinement impact on primary hippocampal astrocyte morphology, cytoskeleton and spontaneous calcium wave signalling *Cells* **12** 293

[25] Singh A V *et al* 2012 Bottom-up engineering of the surface roughness of nanostructured cubic zirconia to control cell adhesion *Nanotechnology* **23** 475101

[26] Wegner K, Piseri P, Tafreshi H V and Milani P 2006 Cluster beam deposition: a tool for nanoscale science and technology *J. Phys. D: Appl. Phys.* **39** R439–59

[27] Tafreshi H V, Piseri P, Benedek G and Milani P 2006 The role of gas dynamics in operation conditions of a pulsed microplasma cluster source for nanostructured thin films deposition *J. Nanosci. Nanotechnol.* **6** 1140–9

[28] Barabási A-L and Stanley H E 1995 *Fractal Concepts in Surface Growth* (Cambridge: Cambridge University Press)

[29] Borghi F, Mirigliano M, Dellasega D and Milani P 2022 Influence of the nanostructure on the electric transport properties of resistive switching cluster-assembled gold films *Appl. Surf. Sci.* **582** 152485

[30] Borghi F, Podestà A, Piazzoni C and Milani P 2018 Growth mechanism of cluster-assembled surfaces: from submonolayer to thin-film regime *Phys. Rev. Appl.* **9** 044016

[31] Borghi F, Sogne E, Lenardi C, Podestà A, Merlini M, Ducati C and Milani P 2016 Cluster-assembled cubic zirconia films with tunable and stable nanoscale morphology against thermal annealing *J. Appl. Phys.* **120** 055302

[32] Mirigliano M, Borghi F, Podestà A, Antidormi A, Colombo L and Milani P 2019 Non-ohmic behavior and resistive switching of Au cluster-assembled films beyond the percolation threshold *Nanoscale Adv.* **1** 3119–30

[33] Gogoi H J and Mallajosyula A T 2021 Enhancing the switching performance of $CH_3NH_3PbI_3$ memristors by the control of size and characterization parameters *Adv. Electrochem. Mater.* **7** 2100472

[34] Yu Y, Wang C, Wen Y, Jiang C, Abrahams I, Du Z, Sun J and Huang X 2022 Realization of volatile and non-volatile resistive switching with N-TiO_2 nanorod arrays based memristive devices through compositional control *J. Alloys Compd.* **909** 164743

[35] Chang T, Jo S-H and Lu W 2011 Short-term memory to long-term memory transition in a nanoscale memristor *ACS Nano* **5** 7669–76

[36] Giotis C, Serb A, Stathopoulos S, Michalas L, Khiat A and Prodromakis T 2020 Bidirectional volatile signatures of metal–oxide memristors—part i: characterization *IEEE Trans. Electron Devices* **67** 5158–65

[37] McGaugh J L 2000 Memory—a century of consolidation *Science* **287** 248–51

[38] Zucker R S and Regehr W G 2002 Short-term synaptic plasticity *Annu. Rev. Phys.* **64** 355–405

[39] Catterall W A and Few A P 2008 Calcium channel regulation and presynaptic plasticity *Neuron* **59** 882–901